IEEE Access
Multidisciplinary | Rapid Review | Open Access Journal

Received December 13, 2019, accepted January 8, 2020, date of publication January 13, 2020, date of current version January 24, 2020.

Digital Object Identifier 10.1109/ACCESS.2020.2966323

Optical Sectioning Microscopy Through Single-Shot Lightfield Protocol

E. SÁNCHEZ-ORTIGA, G. SCROFANI, G. SAAVEDRA, AND M. MARTINEZ-CORRAL
3DID Laboratory, Department of Optics, University of Valencia, E46100 Burjassot, Spain

Corresponding author: G. Scrofani (scrofani@uv.es)

This work was supported in part by the Ministerio de Ciencia, Innovación y Universidades, Spain, under Grant RTI2018-099041-B-I00, and in part by the Generalitat Valenciana, Spain, under Grant PROMETEO/2019/048. The work of G. Scrofani was supported by the Predoctoral contract from EU H2020 Program under grant 676401 (MSCA). The work of E. Sánchez-Ortiga was supported by the Postdoctoral Contract to Generalitat Valenciana, under Grant INNVAL10/19/006.

ABSTRACT Optical sectioning microscopy is usually performed by means of a scanning, multi-shot procedure in combination with non-uniform illumination. In this paper, we change the paradigm and report a method that is based in the lightfield concept, and that provides optical sectioning for 3D microscopy images after a single-shot capture. To do this we first capture multiple orthographic perspectives of the sample by means of Fourier-domain integral microscopy (FiMic). The second stage of our protocol is the application of a novel refocusing algorithm that is able to produce optical sectioning in real time, and with no resolution worsening, in the case of sparse fluorescent samples. We provide the theoretical derivation of the algorithm, and demonstrate its utility by applying it to simulations and to experimental data.

INDEX TERMS Fourier integral microscope, fourier lightfield microscope, FiMic, GPU computing, lightfield microscope, optical sectioning, realtime algorithm.

I. INTRODUCTION

In the past few decades integral (or lightfield) imaging has been proven to be a successful alternative to conventional photography [1]–[7]. Due to its inherent multi-perspective nature, the spatial and the angular information of rays proceeding from a given scene are mixed in the so-called integral image. This spatio-angular information can be exploited in several ways, for instance, the calculation of the depth map [8]–[11], but it is a time consuming process. Also a computational refocusing of the scene to different depth planes can be carried out [12], [13]. The main problem is that the refocused depth images lack of optical sectioning. This happens because any computed depth image integrates rays proceeding from the entire 3D scene. Then, out-of-focus light is not rejected, and the refocused images have a misty appearance, with worsened contrast. This is not a particularly serious problem in macroscopic photography, in which 3D scenes are usually composed of a set of solid non-translucent elements. However, the lack of optical sectioning is a crucial problem in the case of brightfield or fluorescent microscopy, when working with thick samples. This issue is behind the reason for the inception of an increasing number of 3D microscopy techniques in recent decades [14]–[20]. Most of them require a scanning procedure that can be achieved with the movement of the sample or by the deflection of the illumination beam. The drawbacks are that the mechanical movement can damage the sample, introduce distortions due to sample vibrations, and slow down the acquisition, hindering the detection of highly-dynamic biological processes.

In recent years, some techniques have been proposed in order to avoid the axial scanning of the sample. For instance, by means of a confocal microscope with two pinholed detectors of different sizes, the relative decay of the intensity of a given object can be measured depending on its axial position [21]. Once this intensity dependence with the axial position is known, a single transverse image provides information of the axial position of the sample depending on the intensity measurements. Similarly, the depth information can be encoded in a confocal microscope by means of a self-interference set-up [22]. In this case, the collected light passes through a phase plate that creates two alternative optical paths, resulting into an interference pattern in the detector plane. The relative phase of the pattern depends on the axial position of the emitter. Hence, by measuring the phase-shift of the pattern the axial position can be determined without an axial scanning. Other possibility is to use an axial dependent point spread function, particularly, a double-helix

The associate editor coordinating the review of this manuscript and approving it for publication was Md. Asikuzzaman.

function generated by introducing aberrations in the aperture stop of the microscope objective [23]. The angle of the helix generated in the image plane depends on the axial position of the object. Thus, the axial position of a given emitter can be measured by means of the relative angle of the point spread function generated in the image plane. Due to the limited application of this technique to spatially separated point emitters, this procedure is especially suitable for particle localization techniques such as photo-activated localization microscopy (PALM) and stochastic optical reconstruction microscopy (STORM). In these techniques, the probability of having two adjacent molecules simultaneously emitting is virtually zero. The position of different individual emitters is localized at different times, hence, even though 3D information can be obtained by means of a single-shot, these technique require thousands of realizations in order to provide a single 3D image of the sample, which make them unfeasible for real-time acquisition. Note that, all these techniques require the measurement of external parameters: relative intensity of two detectors and the axial response, phase-shift of the self-interference pattern and angle of the aberrated point spread function.

More recently, a new technique has been reported for the direct capture, after a single shot, of multiple orthographic perspective views of 3D microscopic samples. We refer to the so-called Fourier-domain Integral Microscope (FiMic) [24], [25]. FiMic is a lightfield microscope that, compared with precedent versions of lightfield microscopes [26]–[30], provides an improved resolution and depth of field.

Several computational algorithms for refocusing to different depth planes have been reported [26], [27], [31]–[34], but they lack optical sectioning. Recently, a new algorithm [35] that permitted the computational removal of out-of-focus light was published. It is based on the 3D deconvolution between the stack of refocused depth images and a synthetic 3D point spread function (PSF) [34], [35]. This algorithm, however, has the drawback of requiring long calculation time, and of providing important background noise typically inherent to deconvolution procedures.

In this paper, we present a new protocol for obtaining optically-sectioned 3D images in real time. This procedure overcomes the drawbacks described above, and it is well suited for the case of fluorescent, sparse, 3D microscopic samples. Although the procedure is designed for its direct application to the orthographic views captured with a FiMic architecture, it could also be applied to the sub-images that are computed from the micro-images captured with a conventional lightfield microscope. The reported method is supported by the derivation of the theoretical formalism as well as by simulations and laboratory experiments.

II. THEORY

Let us consider a FiMic working in fluorescence mode, as shown in Fig. 1, that provides at the camera plane a set of orthographic views, or elemental images (EIs), of the sample.

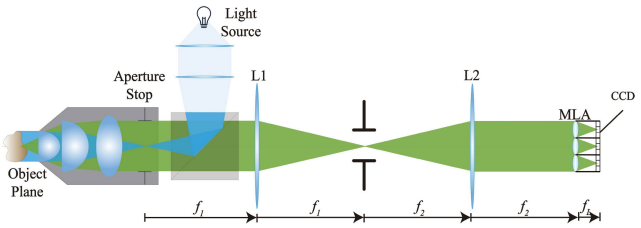

FIGURE 1. Scheme of a Fourier-domain integral microscope (FiMic) working in fluorescent mode.

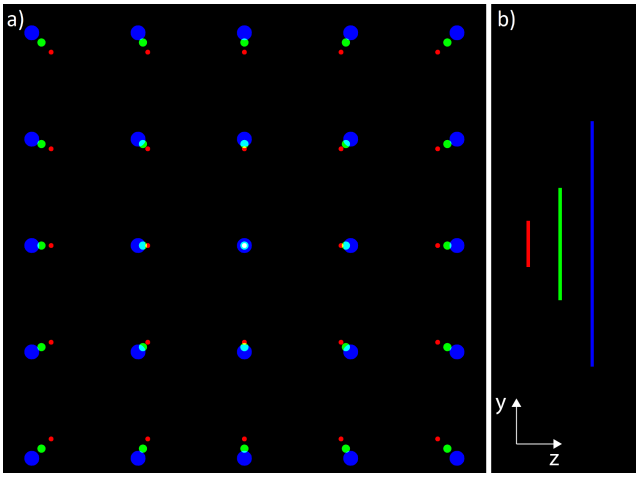

FIGURE 2. a) Simulated integral images of a computationally generated scene for 5x5 EIs. b) Lateral view of the simulated circles.

In order to develop our mathematical model, we assume that: (1) the point spread function (PSF) at the camera plane is smaller than the pixel size; (2) the 3D sample lays within the depth of field of the system; and (3) all the orthographic view images contain the entire sample. Conditions (1) and (2) are true in most practical cases due to the nature of FiMic, and permit to neglect the diffraction effects in the mathematical model. As usual in any lightfield realization, the third condition may not be matched in practice, especially for details close to the limit of the field of view (FOV) in some EI.

The final capture, which we name as the integral image, is composed by a set of EIs that have different perspectives of the object. The 3D intensity distribution in the image space can be expressed in terms of a para-periodic function with different periodicities that depend on the axial position in the object space [18], that is

$$\mathrm{I}(\mathbf{x}, \mathrm{z}) = \sum_{\mathbf{m}} \mathrm{O}(\mathbf{x}, \mathrm{z}) \otimes \delta(\mathbf{x} - \mathbf{m}\alpha\mathrm{z}). \tag{1}$$

Here $\mathbf{x} = (\mathrm{x}, \mathrm{y})$ are the transverse spatial coordinates, z is the axial coordinate as measured from the lenslets focal plane, and O() is the object 3D irradiance distribution. Furthermore, $\mathbf{m} = (\mathrm{m}_x, \mathrm{m}_y)$ is a vector that accounts for the index of a given microlens, and α is the disparity angle. The product between this angle and z gives the disparity suffered by any depth section of the 3D object at any EI. In this equation

we have omitted the magnification factor between object and image plane. This omission has no impact over the rigor of the formalism, but permits to write the equations in clearer form. The 2D irradiance distribution at the camera plane is given by the projection of Eq.(1) over (x, y),

$$\mathrm{I_{EIs}}(\mathbf{x}) = \sum_{\mathbf{m}} \int_{\mathrm{z}} \mathrm{O}(\mathbf{x} - \mathbf{m}\,\alpha \mathrm{z},\, \mathrm{z})\mathrm{dz} = \sum_{\mathbf{m}} \mathrm{I_m}(\mathbf{x}), \tag{2}$$

where $\mathrm{I_m}(\mathbf{x})$ is the irradiance distribution on the $\mathbf{m}$-th EI.

A. THE STANDARD RECONSTRUCTION ALGORITHM

The standard procedure is based on the back-projection and integration of the EIs. Although there are some different algorithms for implementing the procedure [26], [27], [31]–[34], the simplest one is based in shifting and summing (S&S) EIs. To implement this algorithm we need to define the shifting vector $\mathbf{s} = (\mathrm{s}_x, \mathrm{s}_y)$, and the axial parameter, Δ_r. The first defines the shifting direction depending on the position of the EI, whilst the latter represents the amount of shifting that must be applied. Then the refocused irradiance distribution at a given depth plane is given by

$$\mathrm{I_r}(\mathbf{x},\, \Delta_\mathrm{r}) = \frac{1}{\mathrm{N}} \sum_{\mathbf{s}} \mathrm{I_s}(\mathbf{x}) \otimes \delta(\mathbf{x} + \mathbf{s}\,\Delta_\mathrm{r}), \tag{3}$$

where $\mathrm{I_s}(\mathbf{x})$ is the EI whose central position, at the integral image, is given by the vector $\mathbf{s}$. In a practical case, the shifting vector can be measured accurately by detecting the relative positions of the centre of each EI. In such a case, the assumption $\mathbf{m} = \mathbf{s}$ holds and then Eq.(3) results in the following 2D intensity distribution

$$\mathrm{I_r}(\mathbf{x},\, \Delta_\mathrm{r}) = \mathrm{O}(\mathbf{x},\, \Delta_\mathrm{r}) + \frac{1}{\mathrm{N}} \left[\sum_{\mathbf{s}} \mathrm{O}(\mathbf{x} + \mathbf{s}(\Delta_\mathrm{r} - \alpha \mathrm{z}) \right]_{\mathrm{z} \neq \frac{\Delta_\mathrm{r}}{\alpha}} \tag{4}$$

with $\mathrm{N} = \mathrm{N_x} \times \mathrm{N_y}$ being the total number of microlenses. In this formula we find one term that represents the refocused irradiance at the axial depth $\mathrm{z_r} = \Delta_\mathbf{r}/\alpha$. Nevertheless, the rest of the planes are still present in the final image, as deducted from the second term in Eq.(4). This second term is far from being negligible when compared with the first one. As result, the standard refocusing method does not provide optical sectioning since in that case the out-of-focus planes strongly affect to in-focus irradiance distribution.

B. THE S&M RECONSTRUCTION ALGORITHM

The main outcome of this paper is the design and development of a new algorithm that is especially adapted for providing 3D reconstructions of sparse fluorescent samples with optical sectioning. Note that in fluorescence microscopy the illumination light is blocked out by means of a dichroic filter, so that the light reaching the sensor proceeds strictly from the fluorophores. In absence of noise, the regions of the EIs in which the sample is not present are completely dark. Taking advantage of this property as well as the disparity provided by the FiMic, we define the shift and multiply (S&M) method as follows:

$$\mathrm{I_r}(\mathbf{x},\, \Delta_\mathrm{r}) = \left(\prod_{\mathbf{s}} \mathrm{I_s}(\mathbf{x}) \otimes \delta(\mathbf{x} + \mathbf{s}\,\Delta_\mathrm{r}) \right)^{1/\mathrm{N}} \tag{5}$$

where the shifting vector $\boldsymbol{s}$ and the reconstruction parameter Δ_r have the properties previously defined. As in the previous case, it is straightforward to find that

$$\mathrm{I_r}(\mathbf{x},\, \Delta_\mathrm{r}) = \left[\mathrm{O}(\mathbf{x},\, \Delta_\mathrm{r})^\mathrm{N} + \left[\prod_{\mathbf{s}} \mathrm{O}(\mathbf{x} + \mathbf{s}(\Delta_\mathrm{r} - \alpha \mathrm{z}) \right]_{\mathrm{z} \neq \frac{\Delta_\mathrm{r}}{\alpha}} \right]^{1/\mathrm{N}} \tag{6}$$

In Eq.(6) we can distinguish two terms. The first one is the in-focus image, corresponding to the depth distance Δ_r, to the Nth power. The second one is the cross product of N out-of-focus shifted images. For sparse samples, such as disperse particles or thin fibers, the following assumption holds

$$\mathrm{O}(\mathbf{x},\, \Delta_\mathrm{r})^\mathrm{N} \gg \left[\prod_{\mathbf{s}} \mathrm{O}(\mathbf{x} + \mathbf{s}(\Delta_\mathrm{r} - \alpha \mathrm{z}) \right]_{\mathrm{z} \neq \frac{\Delta_\mathrm{r}}{\alpha}}, \tag{7}$$

so that

$$\mathrm{I_r}(\mathbf{x},\, \Delta_\mathrm{r}) = \mathrm{O}(\mathbf{x},\, \Delta_\mathrm{r}) + \mathrm{B}(\mathbf{x},\, \Delta_\mathrm{r}), \tag{8}$$

being $\mathrm{B}(\mathbf{x},\, \Delta_\mathrm{r})$ a low background irradiance noise, which is negligible for sparse fluorescent samples. Strictly, the term $\mathrm{B}(\mathbf{x},\, \Delta_\mathrm{r})$ is a combination of a number of 2s terms that have information of non-focal planes, resulting from the expansion of the Eq.(5). Under the considered conditions, each one of those terms would have a relative weight negligible compared to the intensity contribution of the in-focus plane. Thus, the S&M reconstruction method provides optical sections of the sample located at depths Δ_r. Note that the level of noise depends on the number of views used as well as the sample composition. The sectioning capability is determined by the maximum disparity angle $\alpha_{\max}$ and the lateral dimension of the object δ_{ob}. The axial thickness of the optical section can be evaluated as:

$$\rho_\mathrm{z} = \delta_{\mathrm{ob}} / \tan(\alpha_{\max}). \tag{9}$$

III. RESULTS

In this section, we first present some computer-simulated experiments to prove the validity of the approach. In the second step, we report the results of lightfield experiments, using different 3D fluorescent samples, which demonstrate the utility of our method.

A. SIMULATION

We performed a set of simulations in which, by means of Eq.(1), we calculated the field intensity captured by a FiMic. First, we generated computationally a 3D synthetic scene consisting of three circles of different colors and sizes placed at different axial planes in the object space. The resulting

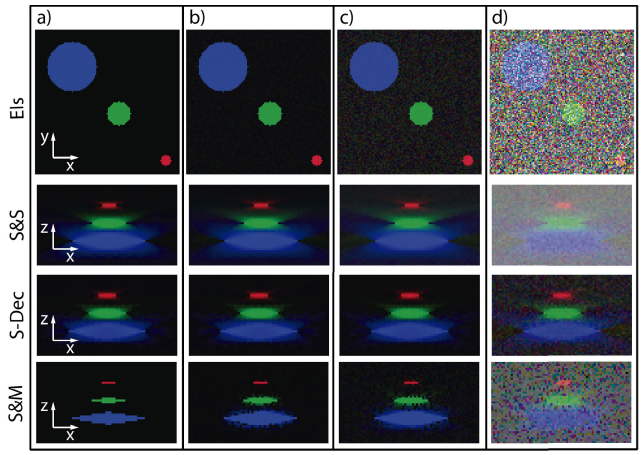

FIGURE 3. Outputs of the tree algorithms when the background noise influence the reconstruction. In the first row we show one of the EIs (the one at the top left corner) used for the calculations. The different cases represent: a) noise free; whilst cases b) c) and d) represent respectively noise levels quantized by the ratio n_{max}/n_{gauss} equal to 10, 5 and 1.

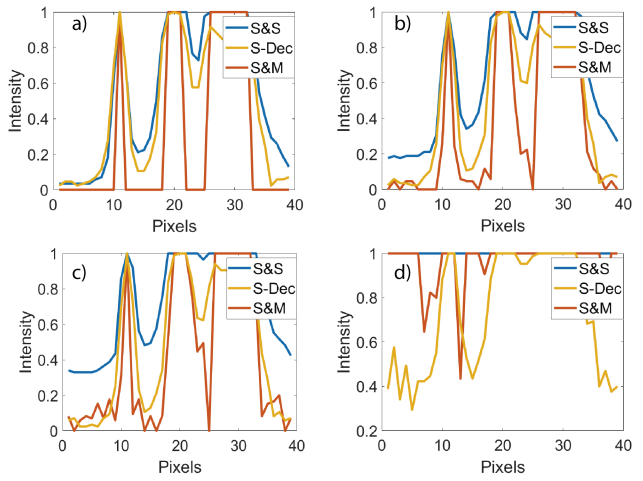

FIGURE 4. Intensity profile along a line passing through the center of the reconstructions outputs of Fig. 3. The background noise influence on the three reconstruction algorithms. The different cases represent: a) noise free; while cases b) c) and d) represents respectively when the ratio n_{max}/n_{gauss} is equal to 10, 5 and 1.

integral image for 5x5 EIs is shown in Fig. 2. Then we applied for a total of 55 axial planes the standard S&S approach, the proposed S&M, and also the algorithm proposed in [35], which we name here as S-Dec. The three z-stacks were 3D rendered by means of a maximum intensity projection (MIP) algorithm. It is apparent from Fig. 3 (a) that the proposed S&M method is the most efficient in the elimination of light proceeding from out-of-focus planes, which instead is present in the standard S&S algorithm, and also the S-Dec shows background noise in the out of focus planes, due to deconvolution procedures. Consequently, a sharper 3D reconstruction of the simulated scene is successfully obtained by S&M.

In order to reinforce this conclusion in Fig. 4 we have drawn the intensity profiles along the straight line passing through the centers of the rendered circles. In particular, in Fig. 4 (a) we see that the red curve (S&M) shows a considerably higher contrast than the curves corresponding to the other methods.

B. NOISE TOLERANCE ANALYSIS

In this section we study the robustness of the S&M algorithm in the presence of noise and compare it to the standard S&S method. Note that the S-Dec algorithm uses a Wiener filter that is tolerant to noise. In order to carry out this study in a microscopy context let us consider the following assumptions. The maximum expected number of photons (n_{max}) coming from the sample and reaching the detector are the same for every elemental image. The shot-noise contribution (Poison noise) has a maximum number of photons of $\sqrt{n_{max}}$. In addition to the shot-noise, a Gaussian noise affects the elemental images as a background with a maximum number of photons of n_{gauss} and a standard deviation of σ_{noise}. Taking these assumptions into account, we simulated the acquisition of a set of 5x5 EIs in low-photon conditions, varying the relationship between maximum expected number of photons with respect to the maximum number of background photons. In Fig. 3 and 4 we represented different reconstructions of the synthetic object for the three methods under study. From the results we can conclude that the background noise affects the final reconstruction quality. The S&M presents a background but the optical sectioning is still achieved even in unpractical conditions ($n_{max}/n_{gauss} = 1$). The S-Dec method shows more tolerance to the background noise level. However, is superior to the S&M only in extreme noise condition. This tolerance is expected from the use of a Wiener filter, which is noise tolerant. It must be underlined that the quality of this reconstruction is dependent on the Wiener parameter, which needs several iteration to be optimized. Therefore, the computation time suffers a huge increase. On the other hand, the S&M increases the signal-to-noise ratio (SNR) of the reconstruction in comparison to the S&S. This effect can be explained since the S&M reduces the global contribution of the background noise from all the EIs whereas in the S&S method the noise of the reconstruction represents an average of the noise contribution from the EIs.

C. RESOLUTION VS. OPTICAL SECTIONING

In the proposed method, there is a trade-off between the optical sectioning and the lateral resolution provided by the system. In order to quantify this relationship, by means of Eq. (9), we calculated the lateral resolution and the optical sectioning as a function of the number of EIs, see Fig. 5. Note that both the lateral resolution and the optical sectioning (OS) are calculated in terms of the ratio to the maximum achievable values. We define these relative values as the factor γ. Note that the number of EIs refers to the number of mililenses in one transverse direction. Furthermore, we represented a set of curves for different sizes of the object, expressed in terms of the percentage of the FOV occupied by the object. As seen from the curves, for point objects the optimal condition in

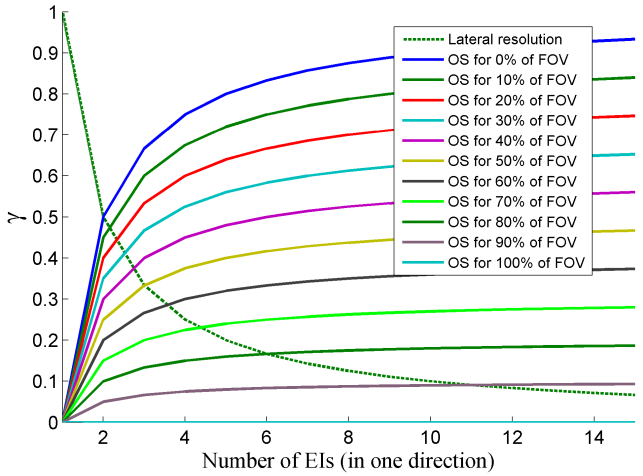

FIGURE 5. Curves of the γ value for the lateral resolution and optical sectioning as a function of the number of EIs and the field-of-view occupied by the sample.

terms of both resolution and optical sectioning occurs for a case between 2x2 and 3x3 mililenses. This can be explained as for a 2x2 EIs the reduction in lateral resolution is minimum while providing some optical sectioning. Even though the optimal condition depends on the size of the object, in practical cases, the details of a sparse sample will not exceed a 10% of the FOV. As expected, increasing the size of the object produces a proportional reduction of the optical sectioning capability.

D. EXPERIMENTAL VERIFICATION

To perform the experimental validation of the theory, we first implemented the Fourier lightfield microscope. Following the scheme shown in Fig. 1, the FiMic consisted of an infinite-corrected microscope objective (20x NA $=$ 0.5), an optical relay of lateral magnification 0.5x ($f_1 = 200$mm and $f_2 = 100$mm), and an array of lenslets of $f = 6.5$mm and pitch p $=$ 1mm (APH-Q-P1000-R2.95 manufactured by AMUS). The optical relay provides the image of the aperture stop onto the lens array so that approximately twelve EIs could be captured by the camera (EO-5012c 1/2") with 2560x1920 square pixels of $\delta = 2.2\mu$m. The effective NA of the system was 0.1 and the total magnification in each EI was 1.3. A mercury lamp and a dichroic filter cube with cut-off frequency $\lambda_c = 505$nm were used for illuminating the sample and collecting the resulting fluorescent light.

With this setup, we captured an integral image of a 3D sample consisting of a number of fluorescent beads (Thermo Scientific Fluoro-Max microspheres 35-14B and 35-9B) of different sizes (ranging for 10 to 100μm) floating in water. The integral image is shown in Fig. 6. Next, we computed 25 refocused depth planes by means of the three algorithms, and applied a maximum intensity projection (MIP) algorithm to obtain a 3D render. The total volume of the resulting 3D refocused image was 811x811x212μm with a voxel size of 1.69x1.69x8.46μm. In Fig. 7 we show three orthographic perspectives of the rendered 3D images obtained with the

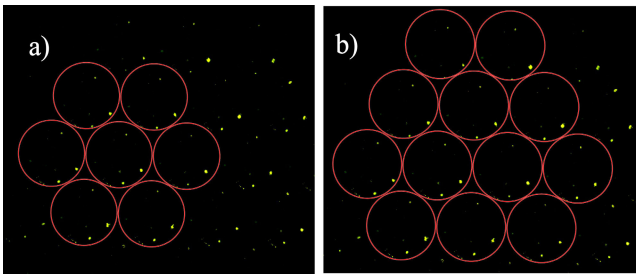

FIGURE 6. Elemental images captured by the sensors. In a) and b) the algorithm respectively selected 7 and 12 EIs.

three algorithms and by using 7 and 12 EIs. Looking at the (x, y) views we can clearly see that the S&M images of the beads are free of out-of-focus light. This is a proof of the optical sectioning capacity of S&M. This effect is reinforced in the case of 12 EIs. Note that the optical-sectioning capability is useful even for improving the lateral resolution. These statements are confirmed by the results shown in the (x, z) and (y, z) views. In these views we see that in case of S&M protocol, the 3D images of the beads are confined to a small volume, and do not show blurry stacks. From these results we confirm the superiority, in terms of optical sectioning, of the proposed protocol over previous proposal for the 3D rendering. Another interesting outcome is that, as expected, the higher the number of views the better the axial resolution.

Note that the derived equations of the S&M considered an object that is present in the FOV of every millilens. In practice, details that are close to the limit of the FOV of a given millilens could not be present in every elemental image depending on the parallax of the axial plane in which they are located. In such case, those details are not present in the final reconstructed image narrowing the effective FOV on the 3D rendered image.

We performed a second experiment, but using different setup and sample. This time we used a microlens array with $f = 5.25$mm and $p = 1$mm (APO-Q-P1000-R2.4 manufactured by AMUS); and a CMOS sensor (DFM 37UX264-ML) with 2448x2048 square pixels of $\delta = 3.45\mu$m in side. As sample we used cotton fibers stained with a solution of Rhodamine 123. After capturing the integral image, made of 25 EIs, the three algorithms under comparison have been applied. The total volume of the resulting 3D image was 969x969x328μm with a voxel size of 3.28x3.28x16.4μm. Also in this case, as Fig. 8 shows, the S&M performs a much better optical sectioning, as result of the efficient removal of the background noise proceeding from the out-of-focus planes. To confirm it, we also depicted an axial response curve for the beads and the fibers in Fig. 9. All the results are shown with their real color and contrast as captured by the sensor and processed by the different algorithms. The videos in Visualisation-1 and Visualisation-2, show respectively the reconstruction of the beads and the fibers for the three algorithms. In the videos the noise removal is much more apparent than in Fig. 7 and Fig. 8.

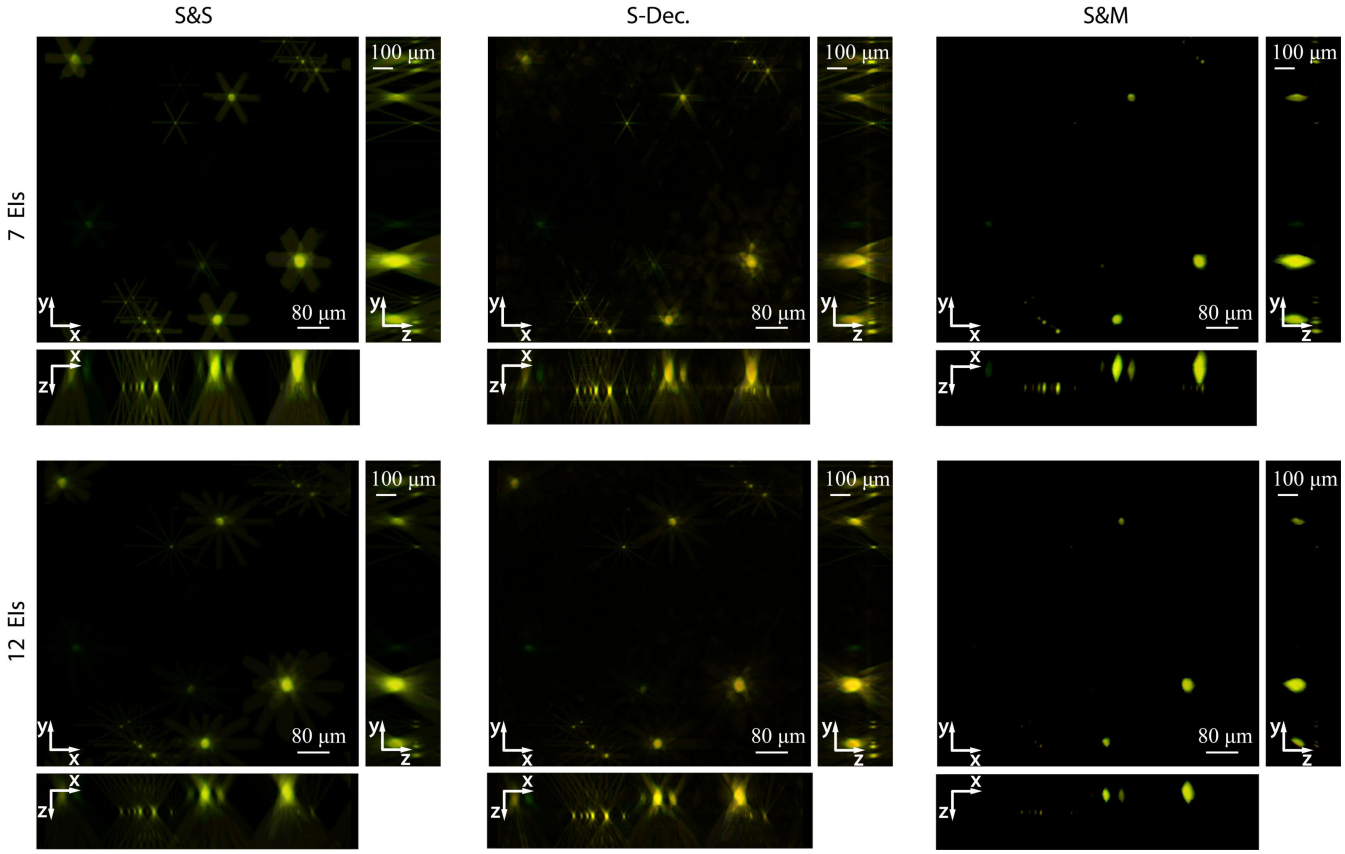

FIGURE 7. Front and lateral views of the simulated 3D render obtained from a z-stack calculated using the S&S backpropagation method (left) the S-Dec (central) and the S&M (right) for 7 and 12 EIs, respectively on top and bottom row.

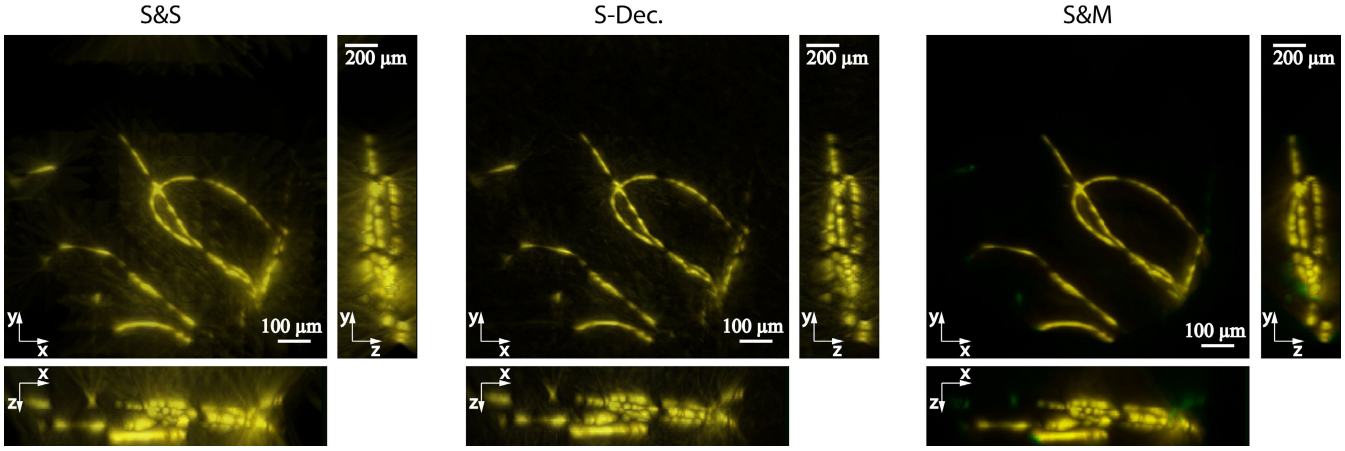

FIGURE 8. Comparison of different methods applied to cotton fibers reconstruction.

IV. GPU ACCELERATED ALGORITHM

As a final step, the computation of the S&M algorithm was implemented in C++ by using CUDA GPU-parallel-computing for real-time performance. As the name of the algorithm already suggests (Shift&Multiply), the function of the algorithm is to shift the elemental images towards a central one, and then multiply the superimposed pixels and normalize the result. Although any EI can be selected as the central one (c-EI) for the algorithm, it is convenient to choose one in the middle of the capture. Once the c-EI is automatically defined by the algorithm and the vector m is known, the remaining algorithm steps are executed with just one parallel function. Each voxel of the resulting volume is independent from the others, therefore Eq.(5) can be computed asynchronously in parallel in the GPU cores.

This dramatically speeds up the reconstruction and opens the doors to possible real-time applications. This real-time

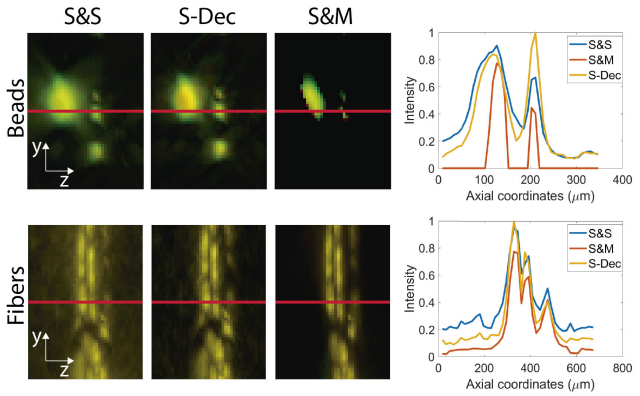

FIGURE 9. Axial curve response for the three different algorithms, for the experiment with the beads (top row) and the fibers (bottom row). The plots represent the intensity of the images along the red line.

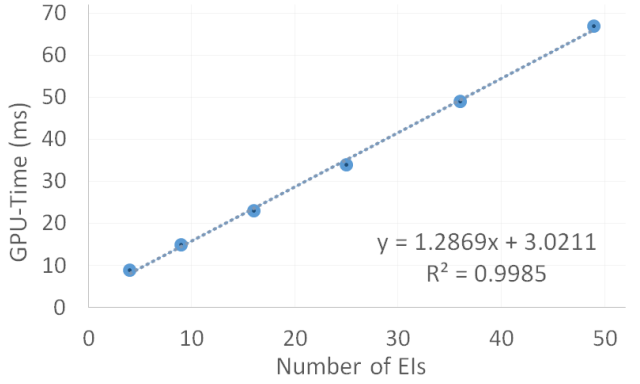

FIGURE 10. The speed of the algorithm is linearly dependent on the number of EIs used in the reconstruction, and is shown with experimental data fitted with a linear curve.

capability could allow, for example, projecting in a 2D monitor only the portion of the sample at a desired depth-plane.

In order to have a deeper knowledge about the algorithm speed, we evaluated the computation times (which are of the order of some tens of milliseconds) as function of the number of EIs involved, and found a linear dependence, see Fig. 10. We can conclude that the higher the number of EIs the better the optical sectioning, but the worse the resolution and the computation time. Then, the adequate selection of the number of EIs is a trade-off process, which is strictly dependent on the specimen under inspection. If more optical sectioning is needed, it will be necessary to scarify speed, or vice versa. Regarding the computational speed with respect to the other two algorithms, it can be said that the processing time is equivalent to the S&S since parallel processing can also be applied in this case. S-Dec requires, first, the calculation of a whole volume from the sample and, after that, a 3D deconvolution with the impulse response. Hence, the number of calculation is significantly higher in S-Dec and, in addition, the 3D deconvolution cannot be parallelized and requires around six seconds to process in the examples treated in this paper. As a consequence, this method is not suitable for

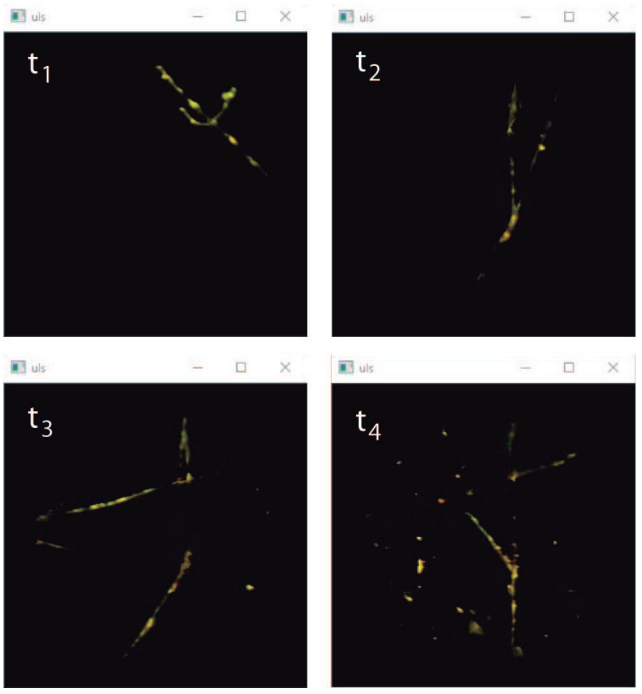

FIGURE 11. Different time-frames extracted from the depth-sectioning video in Visualisation-3.

real-time applications. As an example in Visualisation-3 we show a screen video capture of the real-time protocol operation. In the right-hand window we show the 16 orthographic views. In the experiment we gradually displaced the object. In the left window we show the output of the algorithm. Note that at any frame we focus with optical sectioning a different depth slice of the sample. Fig. 11 shows some frame capture of different depth section shown in Visualisation-3.

V. CONCLUSION

Summarizing, in this work we have proposed a new protocol, based on the lightfield concept, for the reconstruction, with optical sectioning capability, of 3D microscopic sparse samples. The protocol starts with the capture, in single shot, of a number of orthographic views by using a FiMic setup. The second part is based in a novel concept in the refocusing algorithm, the shift and multiply. We have shown analytically and experimentally that the reported protocol permits the reconstruction of 3D microscopic samples with optical sectioning in real-time.

ACKNOWLEDGMENT

(E. Sánchez-Ortiga and G. Scrofani contributed equally to this work.)

REFERENCES

[1] G. Lippmann, "Épreuves réversibles donnant la sensation du relief," *J. Phys. Theor. Appl.*, vol. 7, no. 1, pp. 821–825, 1908.
[2] J. Arai, F. Okano, H. Hoshino, and I. Yuyama, "Gradient-index lens-array method based on real-time integral photography for three-dimensional images," *Appl. Opt.*, vol. 37, no. 11, pp. 2034–2045, Apr. 1998.

[3] F. Okano, H. Hoshino, J. Arai, and I. Yuyama, "Real-time pickup method for a three-dimensional image based on integral photography," *Appl. Opt.*, vol. 36, no. 7, pp. 1598–1603, Mar. 1997.

[4] X. Xiao, B. Javidi, M. Martinez-Corral, and A. Stern, "Advances in three-dimensional integral imaging: Sensing, display, and applications," *Appl. Opt.*, vol. 52, no. 4, pp. 546–560, Feb. 2013.

[5] A. Stern, Y. Yitzhaky, and B. Javidi, "Perceivable light fields: Matching the requirements between the human visual system and autostereoscopic 3-D displays," *Proc. IEEE*, vol. 102, no. 10, pp. 1571–1587, Oct. 2014.

[6] M. Martínez-Corral and B. Javidi, "Fundamentals of 3D imaging and displays: A tutorial on integral imaging, light-field, and plenoptic systems," *Adv. Opt. Photon.*, vol. 10, no. 3, pp. 512–566, Sep. 2018.

[7] N. Bedard, T. Shope, A. Hoberman, M. A. Haralam, N. Shaikh, J. Kovačević, N. Balram, and I. Tošić, "Light field otoscope design for 3D *in vivo* imaging of the middle ear," *Biomed. Opt. Express*, vol. 8, no. 1, pp. 260–272, Jan. 2017.

[8] M. Broxton, L. Grosenick, S. Yang, N. Cohen, A. Andalman, K. Deisseroth, and M. Levoy, "Wave optics theory and 3-D deconvolution for the light field microscope," *Opt. Express*, vol. 21, no. 21, pp. 25418–25439, Oct. 2013.

[9] L. Palmieri, G. Scrofani, N. Incardona, G. Saavedra, M. Martínez-Corral, and R. Koch, "Robust depth estimation for light field microscopy," *Sensors*, vol. 19, no. 3, p. 500, Jan. 2019.

[10] J.-H. Park, S. Jung, H. Choi, Y. Kim, and B. Lee, "Depth extraction by use of a rectangular lens array and one-dimensional elemental image modification," *Appl. Opt.*, vol. 43, no. 25, pp. 4882–4895, Sep. 2004.

[11] N. C. Pégard, H.-Y. Liu, N. Antipa, M. Gerlock, H. Adesnik, and L. Waller, "Compressive light-field microscopy for 3D neural activity recording," *Optica*, vol. 3, no. 5, pp. 517–524, May 2016.

[12] A. Hassanfiroozi, Y.-P. Huang, B. Javidi, and H.-P.-D. Shieh, "Hexagonal liquid crystal lens array for 3D endoscopy," *Opt. Express*, vol. 23, no. 2, pp. 971–981, Jan. 2015.

[13] H. Arimoto and B. Javidi, "Integral three-dimensional imaging with digital reconstruction," *Opt. Lett.*, vol. 26, no. 3, pp. 157–159, Feb. 2001.

[14] M. Gu, *Advanced Optical Imaging Theory*, vol. 75. Springer, 2000.

[15] J. B. Pawley, "Fundamental limits in confocal microscopy," in *Handbook of Biological Confocal Microscopy*. Springer, 2006, pp. 20–42, doi: 10.1007/978-0-387-45524-2.

[16] J. Huisken, "Optical sectioning deep inside live embryos by selective plane illumination microscopy," *Science*, vol. 305, no. 5686, pp. 1007–1009, Aug. 2004.

[17] M. Weber and J. Huisken, "Light sheet microscopy for real-time developmental biology," *Current Opinion Genet. Develop.*, vol. 21, no. 5, pp. 566–572, Oct. 2011.

[18] M. A. A. Neil, R. Juškaitis, and T. Wilson, "Method of obtaining optical sectioning by using structured light in a conventional microscope," *Opt. Lett.*, vol. 22, no. 24, pp. 1905–1907, Dec. 1997.

[19] M. G. Gustafsson, L. Shao, P. M. Carlton, C. J. R. Wang, I. N. Golubovskaya, W. Z. Cande, D. A. Agard, and J. W. Sedat, "Three-dimensional resolution doubling in wide-field fluorescence microscopy by structured illumination," *Biophys. J.*, vol. 94, no. 12, pp. 4957–4970, Jun. 2008.

[20] V. P. Tychinskii, T. Vyshenskaya, E. V. Perevedentseva, and S. Nikandrov, "Measurements of submicron structures with the Airyscan laser phase microscope," *Quantum Electron.*, vol. 27, no. 8, p. 735, 1997.

[21] D.-R. Lee, Y.-D. Kim, D.-G. Gweon, and H. Yoo, "Dual-detection confocal fluorescence microscopy: Fluorescence axial imaging without axial scanning," *Opt. Express*, vol. 21, no. 15, pp. 17839–17848, Jul. 2013.

[22] M. De Groot, C. L. Evans, and J. F. De Boer, "Self-interference fluorescence microscopy: Three dimensional fluorescence imaging without depth scanning," *Opt. Express*, vol. 20, no. 14, pp. 15253–15262, Jul. 2012.

[23] S. Quirin, S. R. P. Pavani, and R. Piestun, "Optimal 3D single-molecule localization for superresolution microscopy with aberrations and engineered point spread functions," *Proc. Nat. Acad. Sci. USA*, vol. 109, no. 3, pp. 675–679, Jan. 2012.

[24] G. Scrofani, J. Sola-Pikabea, A. Llavador, E. Sanchez-Ortiga, J. C. Barreiro, G. Saavedra, J. Garcia-Sucerquia, and M. Martínez-Corral, "FIMic: Design for ultimate 3D-integral microscopy of *in-vivo* biological samples," *Biomed. Opt. Express*, vol. 9, no. 1, pp. 335–346, Jan. 2018.

[25] A. Llavador, J. Sola-Pikabea, G. Saavedra, B. Javidi, and M. Martínez-Corral, "Resolution improvements in integral microscopy with Fourier plane recording," *Opt. Express*, vol. 24, no. 18, pp. 20792–20798, Sep. 2016.

[26] M. Cho and B. Javidi, "Computational reconstruction of three-dimensional integral imaging by rearrangement of elemental image pixels," *J. Display Technol.*, vol. 5, no. 2, pp. 61–65, Feb. 2009.

[27] M. Levoy, R. Ng, A. Adams, M. Footer, and M. Horowitz, "Light field microscopy," *ACM Trans. Graph.*, vol. 25, no. 3, pp. 924–934, 2006.

[28] A. Llavador, J. Garcia-Sucerquia, E. Sánchez-Ortiga, G. Saavedra, and M. Martinez-Corral, "View images with unprecedented resolution in integral microscopy," *OSA Continuum*, vol. 1, no. 1, pp. 40–47, Sep. 2018.

[29] K.-C. Kwon, J.-S. Jeong, M.-U. Erdenebat, Y.-L. Piao, K.-H. Yoo, and N. Kim, "Resolution-enhancement for an orthographic-view image display in an integral imaging microscope system," *Biomed. Opt. Express*, vol. 6, no. 3, pp. 736–746, Mar. 2015.

[30] A. Llavador, E. Sánchez-Ortiga, J. C. Barreiro, G. Saavedra, and M. Martínez-Corral, "Resolution enhancement in integral microscopy by physical interpolation," *Biomed. Opt. Express*, vol. 6, no. 8, pp. 2854–2863, Aug. 2015.

[31] S.-H. Hong, J.-S. Jang, and B. Javidi, "Three-dimensional volumetric object reconstruction using computational integral imaging," *Opt. Express*, vol. 12, no. 3, pp. 483–491, Feb. 2004.

[32] L. McMillan and G. Bishop, "Plenoptic modeling: An image-based rendering system," in *Proc. 22nd Annu. Conf. Comput. Graph. Interact. Techn.*, 1995, pp. 39–46.

[33] R. Ng, "Fourier slice photography," *ACM Trans. Graph.*, vol. 24, no. 3, pp. 735–744, Jul. 2005.

[34] A. Llavador, E. Sánchez-Ortiga, G. Saavedra, B. Javidi, and M. Martínez-Corral, "Free-depths reconstruction with synthetic impulse response in integral imaging," *Opt. Express*, vol. 23, no. 23, pp. 30127–30135, Nov. 2015.

[35] E. Sánchez-Ortiga, A. Llavador, G. Saavedra, J. García-Sucerquia, and M. Martínez-Corral, "Optical sectioning with a Wiener-like filter in Fourier integral imaging microscopy," *Appl. Phys. Lett.*, vol. 113, no. 21, Nov. 2018, Art. no. 214101.

E. SÁNCHEZ-ORTIGA received the B.Sc. and M.Sc. degrees in photonics, and the Ph.D. degree in physics from the Faculty of Physics from the University of Valencia, Spain, in 2008, 2009, and 2014, respectively. He has published more than 30 journal articles in the area of optics and photonics. He is the Co-Owner of four patents. He is also a coauthor of a chapter book, and contributed to more than 40 works presented in international conferences.

G. SCROFANI received the B.Eng. degree in biomedical engineering and the M.Sc. degree in electronic engineering from the Polytechnic University of Milan, in 2013 and 2016, respectively. He is currently pursuing the Ph.D. degree with the 3D Imaging and Display Laboratory, University of Valencia, with the aim of developing a plenoptic microscope, funded by the Marie Sklodowska Curie Action (MSCA). His research interests include optics and optoelectronics.

G. SAAVEDRA received the M.Sc. and Ph.D. degrees *(cum laude)* in physics from the University of Valencia, Spain, in 1990 and 1996, respectively. He is currently a Full Professor. Since 1999, he has been the Co-Leader of the 3D Imaging and Display Laboratory, University of Valencia. His research interests are optical diffraction, plenoptic/integral imaging techniques, and 3D high-resolution optical microscopy. He has supervised on these topics seven Ph.D. theses (two of them honored with the Best Thesis Award). He has published about 120 technical articles on these topics in major journals. He has contributed in more than 80 conference proceedings, including more than 50 invited/keynote presentations. He has filed eleven patents on 3D display and imaging techniques.

M. MARTINEZ-CORRAL received the Ph.D. degree in physics from the University of Valencia, in 1993. He is currently a Full Professor of optics with the University of Valencia. He co-leads the 3D Imaging and Display Laboratory. His research interests include resolution procedures in 3D scanning microscopy, and 3D imaging and display technologies. He has supervised on these topics 16 Ph.D. theses (three honored with the Best Thesis Award), published over eighty technical articles in major journals (which received more than 3.000 citations), and pronounced a number of invited and keynote presentations in international meetings. He is also co-inventor of twelve patents, one of them supporting the creation of one Spin-off of the University of Valencia. He was an Elected Fellow of the SPIE in 2010 and a Fellow of the OSA in 2017. He received the Best Thesis Award during his Ph.D. studies. He has been serving as the Program Committee of a number of Conferences sponsored SPIE, OSA, IEEE, and so on. He is currently the Co-Chair of the Three-Dimensional Imaging, Visualization, and Display Conference within the SPIE meeting in defense, security, and sensing. He is also the Topical Editor of the OSA journal *Applied Optics*.